Potential Vorticity Diagnosis of the Severe Convective Regime. Part I: Methodology

DAVID A. GOLD* AND JOHN W. NIELSEN-GAMMON

Department of Atmospheric Sciences, Texas A&M University, College Station, Texas

(Manuscript received 16 November 2006, in final form 30 April 2007)

ABSTRACT

Observational and modeling studies have shown that shear and instability are powerful predictors of the likelihood of severe weather and tornadoes. To the extent that upper-tropospheric forecast errors can be described as potential vorticity (PV) anomalies on the forecasted PV field, knowing (and being able to quantify) the effects of such errors on shear and instability would allow forecasters to anticipate the effects of those errors on the likely mode of severe weather. To test the sensitivity of the severe convective environment to PV fluctuations, a PV inversion framework is adopted that utilizes nonlinear balance. The observed PV field is modified in a way that mimics realistic perturbations of trough intensity, location, or shape. Soundings, including moisture profiles, are reconstructed from the balanced geopotential height field assuming that air parcels conserve mixing ratio while their isentropic surfaces are displaced upward or downward by the addition of anomalous PV. Unperturbed balanced soundings agree reasonably well with full, unbalanced soundings, and differences are attributable to departures from nonlinear balance in areas of strong vorticity or acceleration. Balanced vertical wind profiles do not include the effects of friction, so the vertical shear of the balanced wind departs unacceptably from total shear within the lowest 1 km of the troposphere. The balanced wind perturbations are added to the total analyzed shear profile to estimate the effect of PV perturbations on shear and storm-relative helicity. By this process, the importance of typical or hypothesized upper-tropospheric forecast errors may be addressed in an idealized, case-study, or operational context.

1. Introduction

While individual storms can (and do) exhibit widely varying morphologies and evolutions within a given environment, the basic structure of an environment favorably predisposed to severe thunderstorms is fairly well understood (Doswell 1982). The fundamental components of an atmospheric state supportive of severe thunderstorms are (i) potentially unstable vertical stratification, (ii) the presence of low-level moisture, (iii) a mechanism for lifting low-level air, and (iv) vertical shear of the horizontal winds. A clear understanding of the physical processes responsible for generating these components is a necessary condition for the development of a systematic approach to severe convective forecasting.

Because of advances in subsynoptic-scale numerical modeling and atmospheric remote sensing technology, the focus of severe storm research during the past few decades has shifted to increasingly smaller-scale processes, from the role of synoptic-scale disturbances to that of the mesoscale and storm scale.[1] Despite advances in convective-scale and mesoscale prediction stemming from the above studies, questions remain regarding the link between the larger-scale environment and the mode and intensity of severe convection. Some of the most damaging and violent severe convective events occur within large severe thunderstorm outbreaks, events that are clearly controlled to some degree by the large-scale or background environment. Mesoscale models are also beginning to exhibit skill at forecasting the convective mode more than a day in advance (Fowle and Roebber 2003; Done et al. 2004). Yet, whereas a sizeable proportion of significant tornadoes are associated with an identifiable upper-

* Current affiliation: PPM Energy, Inc., Houston, Texas.

Corresponding author address: David A. Gold, P.O. Box 420898, Houston, TX 77242.
E-mail: dr_david_gold@earthlink.net

[1] For a historical perspective on severe thunderstorm forecasting in the United States, the reader is referred to Schaefer (1986).

DOI: 10.1175/2007MWR2090.1

tropospheric trough, few such upper-level systems lead to significant tornadoes. Any insight into *which* upper-tropospheric disturbances are most likely to contribute to violent severe convective episodes would be of great benefit to the operational forecasting community (R. Thompson 2000, personal communication). Discussing the conditions associated with the worst tornado outbreak in Oklahoma history, that of 3 May 1999, Thompson and Edwards (2000) point out that large-scale pattern recognition based on forecasted upper-level flow fields did not impel forecasters to anticipate a major tornado outbreak. Nevertheless, several key severe weather parameters, as measured by the existing observational network in the outbreak region, turned out to be well within the range typically associated with strong to violent tornadoes.

Even if an upper-level trough is correctly predicted to produce widespread severe weather, it can be problematic to determine the predominant type of severe weather likely to result (Johns and Hart 1993). It is well established that the midtropospheric ascent forced by shortwave troughs and attendant jet streaks, albeit too weak to be proximately responsible for the severe deep moist convection itself, is associated with the development of conditions that ultimately lead to severe storm outbreaks. However, aside from forcing upward vertical motion and despite evidence that the large-scale flow is a controlling factor in many of these events, the extent to which upper-tropospheric troughs promote the emergence of vertical shear and buoyancy distributions conducive to intense convective outbreaks is not clear. It is similarly difficult to determine the relative importance of large-scale and subsynoptic-scale processes in a given scenario (Doswell 1987).

The maturation of techniques for diagnosing the dynamics of large-scale atmospheric disturbances enables new and potentially insightful investigations into the role of mobile upper-level troughs in regulating the severe convective regime (SCR), just as advances in subsynoptic-scale numerical modeling and atmospheric remote sensing have resulted in increased understanding of mesoscale and storm-scale processes. Specifically, potential vorticity (PV) invertibility (Hoskins et al. 1985, hereafter HMR85) makes it possible to retrieve that portion of the total balanced winds and temperature field (and therefore vertical wind shear and CAPE) directly attributable to a given upper-level trough. Moreover, the ability to invert the PV under high-order balance constraints such as nonlinear balance (Davis and Emanuel 1991, hereafter DE91) makes it feasible to use PV invertibility to study phenomena that are poorly approximated by geostrophic balance. Because of the highly ageostrophic nature of the atmosphere associated with the most significant severe weather outbreaks, it is appropriate to use the nonlinear balance (NLB) PV inversion scheme developed by DE91.

This set of papers applies the PV diagnostic framework to investigate how the upper-tropospheric PV anomalies associated with mobile troughs influence the environments in which severe convective outbreaks occur. The goal is to understand the sensitivity of the convective environment to *changes* in the upper-level PV (UPV) distribution, such as whether one particular configuration of PV is more or less favorable than another for the development and severity of the storms. This requires the ability to physically link some measure of the atmosphere's "convective potential," or propensity to support severe convection, to the PV itself. This will be accomplished by computing from the balanced flow variables (retrieved from the PV distribution via PV inversion) certain convective parameters that are known to be correlated with storm severity. Then, for a given UPV change, the corresponding change in those convective parameters can be readily computed.

The purpose of this paper, the first of four companion papers, is to develop the mathematical framework for computing the convective parameters from the balanced flow variables. The approach is general and includes some novel techniques for treating inversions over topography, specifying realistic PV anomalies, and recovering the moisture distribution from the inverted temperature field. A companion paper (Nielsen-Gammon and Gold 2008, hereafter Part II) presents a conceptual framework for interpreting and understanding the role of UPV features in modulating the balanced convective environment. In the subsequent papers (Gold and Nielsen-Gammon 2008a,b, hereafter Part III and Part IV, respectively), the methodology developed in Parts I and II is applied to two tornado outbreaks. The current paper is organized as follows: section 2 describes the dataset and PV inversion scheme used in this study, followed by a description of the procedure used to effect realistic PV modifications needed for Parts III and IV. Section 3 presents the methodology used to compute the convective parameters from the balanced flow fields. Also examined in section 3 is the nature of the unbalanced portion of the flow and its impact on the balanced convective parameters. The methodology presented in this work is summarized in section 4.

2. Data, PV inversion, and PV modification

a. Dataset

The study uses the reanalysis dataset (Kalnay et al. 1996) from the National Centers for Environmental

Prediction (NCEP), created using 28 vertical sigma levels and a T62 trapezoidal spherical harmonic truncation. The data were stored as 6-h global analyses on a Gaussian 192 × 94 grid, which has 1.9° × 1.9° latitude–longitude (211 km × 166 km) grid resolution at 38°N. To facilitate PV calculations and inversions, the data are first transformed to a 1.25° × 1.25° (139 km × 109 km) computational grid and then interpolated vertically from σ- to p-coordinate surfaces at 25-hPa intervals between 1000 and 50 hPa. The variables interpolated by this procedure are geopotential heights (Z), virtual temperature (T_v), specific humidity, and the zonal and meridional wind components (u and v, respectively). All of the above variables, except for the wind components and including pressure, are available at the lowest half-sigma level, which will be taken to be the earth's surface. When needed within this study, surface wind components are computed by means of linear interpolation to the surface pressure level from the nearest bracketing pressure levels. All surface variables are hereafter denoted with a subscript sfc (e.g., $T_{\rm sfc}$).

Vertical interpolation from terrain-following coordinates to pressure surfaces invariably requires the adoption of a strategy for extrapolating data to subterranean grid points since pressure surfaces will intersect the ground in regions of orography. From a PV perspective, subterranean extrapolation of data amounts to creating a fictitious PV field in the computational domain. Using PV thinking (HMR85), it is clear that some portion of the total flow will be attributable to any spurious PV anomaly. While most existing extrapolation schemes aim to estimate as accurately as possible the sea level pressure field, the goals of this study are best served by ensuring that the data are extrapolated so as to minimize the flow attributable to the artificial subterranean PV. In this study and the subsequent papers (Part II, Part III, and Part IV), the reanalysis data are first extrapolated using the so-called Shuell procedure (Mesinger and Treadon 1995) and then postprocessed using a scheme designed to impose balance between the subterranean mass and momentum fields (Gold 2004). The postprocessing replaces static stability profiles in and near elevated orography with the neighboring atmospheric static stability and imposes geostrophic balance on the wind field in this layer. Doing so improves the agreement between actual and inverted fields within the free atmosphere by reducing the response of the above-ground atmosphere to fictitious, below-ground unbalanced PV anomalies during the inversion process.

Since NLB PV inversion, as currently implemented, is designed to operate only over a limited horizontal domain, a subgrid of the global reanalysis dataset is extracted prior to PV inversion. The boundaries of this subdomain are chosen to be 20°N, 177.5°W (lower left corner) and 80°N, 60°W (upper right corner). Treatment of horizontal boundary conditions for the solution of the PV inversion problem is identical to that implemented by DE91. To increase the likelihood that the PV inversion algorithms will achieve numerical convergence, the vertical resolution of the postprocessed reanalysis data described above is halved. The resulting balanced flow fields and their associated PV distributions are thus represented on a vertical grid with 50-hPa resolution.

b. PV inversion scheme

Previous studies employing PV diagnosis have largely focused on the role of various PV anomalies in promoting midlatitude cyclogenesis. To this end, the application of PV attribution has proceeded along two primary avenues: (i) assessing the direct contribution of the static perturbation height and wind anomalies to the cyclogenesis event (e.g., DE91), or (ii) quantifying the relative importance to cyclogenesis of various physical mechanisms associated with PV advection by the basic-state and perturbation balanced wind fields (e.g., Nielsen-Gammon and Lefevre 1996). While there is a well-established protocol for applying PV inversion to the study of the dynamics of midlatitude synoptic-scale storm systems, no comprehensive procedure yet exists for using PV diagnosis to investigate the SCR. Creating such a framework requires linking the UPV to the convective parameters themselves, a task that is achieved by computing the convective parameters in terms of the balanced flow variables obtained via PV inversion. Once the convective parameters are computed from the balanced fields, their distributions can be used in the same manner as their observed counterparts, provided that the balanced parameters comprise the same essential information.

The solution of the NLB system, including a set of time-dependent equations for vertical motion and irrotational flow, yields the following balanced variables for a given distribution of Ertel's PV q: the geopotential heights Φ_B, the nondivergent streamfunction Ψ_B, velocity potential χ, and vertical motion ω. For a detailed description of the NLB PV inversion procedure, the reader is encouraged to consult DE91.

The desire to study the sensitivity of the convective parameters to the structure and geometry of the upper-tropospheric PV distribution motivates a PV partitioning that treats PV changes themselves as perturbations to the unmodified distribution, which in turn serves as the background PV state. This approach differs from the more traditional PV decomposition, in which PV anomalies are defined relative to some arbitrary basic

state (e.g., the time-averaged or low-wavenumber PV; see DE91; Nielsen-Gammon and Lefevre 1996 for examples). Hence, if the initial PV distribution q_0 undergoes a change δq, the modified PV can be expressed as the sum

$$q = q_0 + \delta q. \tag{1}$$

The PV modification δq can subsequently be inverted (using piecewise inversion) to recover the associated balanced flow changes $\delta\Phi_B$, $\delta\Psi_B$, $\delta\chi$, and $\delta\omega$. Thus, one can diagnose the effect on the SCR of modifying the UPV in a specific manner (e.g., amplifying or removing an existing upper-tropospheric trough).

c. PV modification scheme

Here we present a novel methodology for modifying an existing upper-tropospheric PV distribution, q_0. PV modification, also called "PV surgery," is the approach used to examine the sensitivity of the convective parameter space to specific aspects of the UPV in the current study. Unlike the highly simplified idealized experiments to be presented in Part II, the PV surgery procedure described below is designed to create realistic and complex changes to the UPV distribution.

PV surgery is a natural tool of choice for those wishing to understand how a specific PV anomaly influences the outcome of a particular meteorological event. Several recent studies have used PV surgery as a cornerstone of their diagnosis of particular events (Huo et al. 1999; Dickinson et al. 1997; Davis and Bosart 2002). In a study more germane to the current topic, Roebber et al. (2002) both remove and amplify the PV associated with an upper-tropospheric shortwave trough to assess its contribution to the 3 May 1999 Oklahoma tornado outbreak. In each of the studies cited above, the authors were able to quantify the contributions of a specific PV anomaly to a given weather event by removing the PV anomaly in question from the total PV distribution, inverting the remaining PV (or running a simulation initialized with the modified PV field), and examining the results. Thus, PV surgery appears to be suitable as a "poor-man's adjoint" to examine the sensitivity of various atmospheric phenomena to particular features in the upper-tropospheric PV distribution.

PV surgery, as applied in the aforementioned studies, amounts to simply removing or amplifying a specific PV anomaly. In the current study, the goal is to develop a more general approach to PV modification, one in which the geometric distribution of the analyzed PV itself, q_0, can be directly modified without first decomposing the PV distribution into basic-state and perturbation portions, partitioning that inevitably requires making arbitrary choices about how to define the basic state. In this study, the perturbation PV field is simply defined as $\delta q = q_n - q_0$, where q_n is the modified PV distribution.

Altering the geometric configuration of q_0 is tantamount to relocating the PV gradient, requiring the development of a procedure that mimics the rearrangement of PV contours by advection. Repositioning PV contours implies that the new PV values on either side of the gradient must blend in with existing background values. Specifically, q_n values should be everywhere constrained to remain with a range:

$$\min(q_0, q_{\rm tr}) \le q_n \le \max(q_{\rm st}, q_0), \tag{2}$$

where $q_{\rm tr}$ is a typical tropospheric PV value (chosen to be 0.5 PVU) and $q_{\rm st}$ a typical stratospheric value at a given pressure. The constraints (2) permit q_n magnitudes smaller than $q_{\rm tr}$ only at grid points where q_0 itself is smaller than $q_{\rm tr}$, and allow values larger than $q_{\rm st}$ only where q_0 is larger.

The PV modification procedure used in this work, hereafter called "PVMOD," is given by

$$q_n = \begin{cases} \max\{\min[Hq_0, \max(q_{\rm st}, q_0)], \min(q_0, q_{\rm tr})\} & \text{if} \quad A > 0, \\ \max\{\min[Hq_0, \max(q_{\rm st}, q_0 + 1)], \min(q_0, q_{\rm tr})\} & \text{if} \quad A < 0, \end{cases} \tag{3}$$

where

$$H(x', y', p) = \left(\frac{q_{\rm st}}{q_{\rm tr}}\right)^{A \times g(p) \times S(x', y')},$$

$$S(x', y') = \begin{cases} \dfrac{2}{\sqrt{3}}\,\pi^{-1/4}\left[1 - \dfrac{(x')^2}{a^2} - \dfrac{(y')^2}{b^2}\right] \exp\left\{-\dfrac{1}{\gamma}\left[\dfrac{(x')^2}{a^2} + \dfrac{(y')^2}{b^2}\right]\right\}, (x', y') \in \mathbb{D} \\ 0, \quad \text{otherwise} \end{cases}$$

$$g(p) = \begin{cases} \cos\left[\pi\left(\dfrac{p_0 - p}{400}\right)\right] |p_0 - p| < 200 \text{ hPa} \\ 0, \quad \text{otherwise.} \end{cases}$$

TABLE 1. A lookup table for pressure-level (hPa) average values of stratospheric PV (PVU), q_{st}.

p	500	450	400	350	300	250	200	150	100
q_{st}	1.7	1.8	2.3	2.8	3.8	5.2	6.3	7.7	9.0

In (3), $H(x', y', p)$ is a master amplitude function that governs the amplitude of the PV change, including its geometrical distribution and vertical structure; A is an amplitude exponent ranging from -1 to 1; $S(x', y')$ is a horizontal shape function specifying the geometric region over which the PV modification is applied in a subdomain $\mathbb{D}$ (to be defined below), and $g(p)$ is a vertical structure function specifying the vertical distribution of the change.

The shape function is simply the "Mexican hat" (MH) wavelet (Daubechies 1992), chosen for its desired characteristic of localizing the forcing by causing the function to become slightly negative on either side (in one dimension) of the peak. When perturbing the PV, this produces a ring of oppositely signed PV surrounding the perturbation that, upon inversion, spatially localizes the balanced response to the PV anomaly and results in a fairly rapid horizontal decay in Ψ'. The two-dimensional shape function S' used in (3) is represented parametrically in terms of the Cartesian coordinates of an ellipse $(x'/a)^2 + (y'/b)^2 = 1$ with major and minor axes a and b, respectively, rotated through an angle ϕ relative to the principal axes. The factor $1/\gamma$ is a "rebound" parameter, modulating the rapidity with which the exponential term in S' damps the function to zero away from the sidelobes. The subdomain over which S' is applied is defined to be a rectangle extending four grid points beyond both the semimajor and semiminor axes. The vertical structure function $g(p)$ maximizes the amplitude of the PV perturbation at the desired pressure level p_0, with vertical decay to zero amplitude 200 hPa above and below that level. For most PV modifications, p_0 is chosen to be 300 hPa. The amplitude of the structure function is forced to vanish at altitudes greater than 100 hPa since the PV gradient associated with the jet stream typically disappears at these levels and at pressure levels below 500 hPa where stratospheric PV is relatively scarce.

The amplitude exponent, A, and in particular the ratio, $(q_{st}/q_{tr})^A$, makes it possible to express a new PV distribution q_n as a multiple of the background PV. By allowing A to vary from -1 to 1, the prescribed "forcing" ranges from (q_{tr}/q_{st}) to (q_{st}/q_{tr}), where q_{tr} and q_{st} are typical values of tropospheric and stratospheric PV, respectively, at each pressure level. These values may be case-dependent and should be determined from examination of the PV distribution near the area to be modified. In the computations shown here and in Parts III and IV, $q_{tr} = 0.5$ PVU and the values given in Table 1 were used for q_{st}.

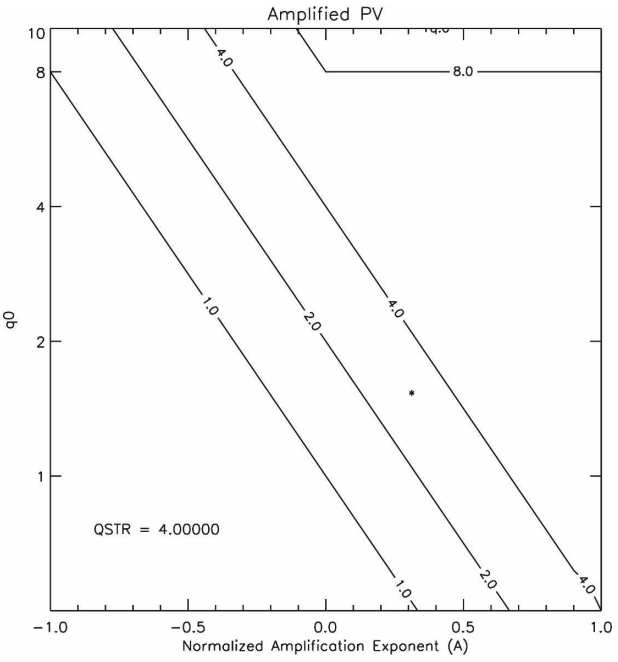

FIG. 1. A plot of q_n as a function of the amplification exponent A and q_0 for the case where $q_{st} = 4.0$. The asterisk represents the value of q_n (3 PVU) when $q_0 = 1.5$ PVU and $A = 0.3$.

A graph of the modified PV amplitudes as a function of q_0 and the exponent A for $q_{st} = 4$ PVU is presented in Fig. 1, which provides an easy way to visualize how the PV's amplitude will change depending on its initial value, and the amount of normalized amplification or reduction is applied. For example, if $q_0 = 1.5$ PVU and $A = 0.3$ at a given grid point where the average stratospheric PV value at that level is $q_{st} = 4$ PVU, the PV is doubled to 3 PVU.

A more general interpretation of Fig. 1 is that the closer to q_{st} the original PV value is at a location, the more impact a reduction in PV amplitude (i.e., negative A) will have and the less impact a PV increase (i.e., positive A) has. The opposite is true for q_0 values close to q_{tr}. The values $q_{tr} = 0.5$ PVU and $q_{st} = 8$ PVU represent limiting "barriers," beyond which no modified PV values are permitted, regardless the values of q_0 and A.

The free parameters in (3) control the amplitude and orientation of a three-dimensional elliptical patch of modified PV. When a simple modification of the PV is desired, the assignment of values to the free parameters is straightforward, and the parameters can be tuned until the desired q_n distribution is obtained.

Relatively complex PV modifications are attainable by changing q_0 over several disparate regions. For example, to transform a positive circular PV patch centered at (x_0, y_0) to an ellipse with the major axis parallel to meridians, one can reduce the PV along the patch's western and eastern edges by applying (3) centered at points $(x_0 - \Delta x, y_0)$ and $(x_0 + \Delta x, y_0)$ using a negative value of A. One can manipulate the ellipticity of the two modifying patches by adjusting the axis parameters (a, b). The optimal locations for applying the elliptical patches can be determined through trial and error by varying Δx.

d. An example of PV modification

A realistic example of PV modification using the PVMOD scheme is presented in Fig. 2. At the time shown, a significant upper-tropospheric trough is located over the central United States, manifested as a pronounced southeastward protrusion of stratospheric PV values at 250 hPa from a local maximum centered over northern Wyoming.

This PV configuration corresponds to what operational meteorologists refer to as a "negative-tilt" trough, and is associated with a significant tornado outbreak in progress over Iowa at the time shown (0000 UTC 8 June 1984). For this example, the PV was modified over an elliptical region centered at 41.25°N, 98.75°W in Fig. 2a using the shape and amplitude parameters displayed in the lower right-hand corner of the panel. The effect of constraining the amplitude of q_n is illustrated by comparing q_n and q_0, both without (Fig. 2a) and with (Fig. 2b) the constraints [(2)]. Unconstrained amplification of the stratospheric protrusion results in a modified PV field (dashed contours) that extends farther southeastward with a new local PV maximum of 9 PVU created over central Nebraska. Moreover, the PV gradient at the periphery of the PV tongue is greatly increased from its background state. When the constraints on q_n are enforced (Fig. 2b), the local maximum present over central Nebraska in Fig. 2a disappears and the PV gradient on the southeastern flank of the PV tongue is effectively moved southeastward. Thus, by constraining the amplitude of the modification, the PV gradient is reconfigured without drastically increasing the PV on either side of the gradient.

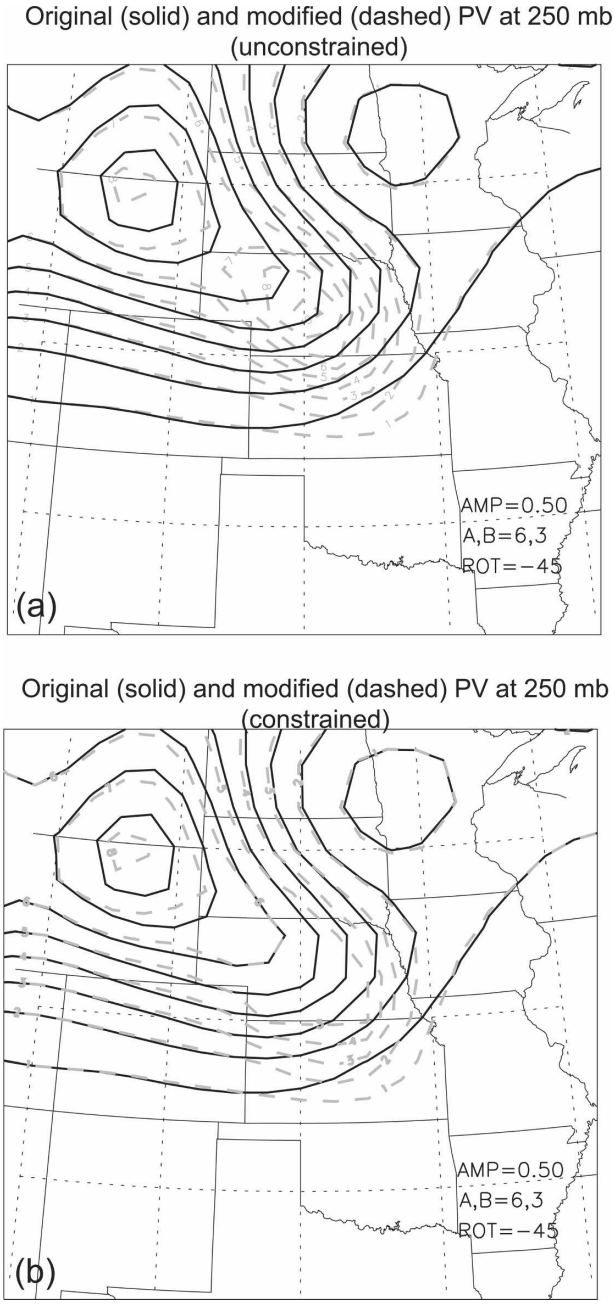

FIG. 2. PV modification example. Unperturbed (q_0, solid black contours) and modified (q_n, dashed gray contours) PV at 250 hPa at 0000 UTC 8 Jun 1984. The modified PV (a) was attained subject to no constraints on its amplification and (b) shows the results of imposing constraints. See text for detailed description of how the modified PV is constrained.

3. Computing the balanced convective parameters

a. Computing the vertical shear parameters from the balanced winds

It has long been established that the mode, intensity, and longevity of thunderstorms are strongly controlled by the amount of buoyancy and vertical wind shear present in the storm environment (Weisman and Klemp 1982). As a result, operational meteorologists employ numerous convective parameters that capture some aspect of the buoyancy, the shear, or both. Sev-

eral parameter studies (Davies and Johns 1993; Rasmussen and Blanchard 1998; Craven et al. 2002) have recently identified several quantities that appear to be most effective at discriminating among the various convective modes (e.g., nontornadic versus tornadic storms): the storm-relative environmental helicity (SREH), the vertical shear (SHR), and the bulk Richardson number shear (BRNSHR). This subset has been demonstrated by the aforementioned parameter studies to have some capability to distinguish between the extreme ends of the convective mode spectrum. Moreover, these parameters are currently among the most widely used in operational forecast settings. Therefore, these are the shear parameters used in this study to characterize the SCR. The conventional formulas for SREH, SHR, and BRNSHR are

$$\mathrm{SREH} = \int_{\mathrm{sfc}}^{z} (\mathbf{V} - \mathbf{C}) \cdot \boldsymbol{\nabla} \times \mathbf{V}\, dz$$

$$= \int_{\mathrm{sfc}}^{z} \mathbf{k} \times \frac{d\mathbf{V}}{dz} \cdot (\mathbf{V} - \mathbf{C})\, dz, \qquad (4)$$

$$\mathrm{SHR} \equiv \|\mathbf{V}_6 - \mathbf{V}_{\mathrm{PBL}}\|, \quad \text{and} \qquad (5)$$

$$\mathrm{BRNSHR} \equiv 0.5 \times (\overline{u}^2 + \overline{v}^2), \qquad (6)$$

where the storm motion vector $\mathbf{C}$ is computed using the method devised by Bunkers et al. (2000), $\mathbf{V}_6$ represents the horizontal wind at 6 km, $\mathbf{V}_{\mathrm{PBL}}$ represents the wind of the planetary boundary layer (PBL) (discussed below), and $\overline{u}$ and $\overline{v}$ represent the components of the difference between the mass-weighted mean winds in the 0–6-km layer and the PBL winds.

In the current study, the shear-related parameters (4)–(6) are calculated in the context of the NLB framework. The prognostic balance equations (PBEs) derived by DE91 are used to obtain the irrotational flow $\mathbf{V}_{B_\chi}$ (see their appendix B), while the nondivergent balanced winds $\mathbf{V}_{B_\Psi}$ are obtained through inversion of the total analyzed PV distribution, $q_{0,}$ using the NLB equations [their Eqs. (2.1) and (2.3)] as well as the same horizontal and vertical boundary conditions. The shear parameters are subsequently computed using the full balanced winds, $\mathbf{V}_B = \mathbf{V}_{B_\Psi} + \mathbf{V}_{B_\chi}$ (Davis et al. 1996).

The $\mathbf{V}_{\mathrm{PBL}}$ is often defined to be the wind averaged over the surface to the 0.5-km layer. In the current study, however, (4)–(6) are computed using $\mathbf{V}_{\mathrm{sfc}}$ in place of $\mathbf{V}_{\mathrm{PBL}}$ because of limited vertical resolution in the analysis and balanced data (25 and 50 hPa, respectively). The balanced surface winds $\mathbf{V}_{B_{\mathrm{sfc}}}$ are obtained by linearly interpolating the balanced winds, which are given at equally spaced pressure surfaces with a 50-hPa interval, to the observed station pressure p_{sfc} from the two pressure levels bracketing p_{sfc} at each grid point.

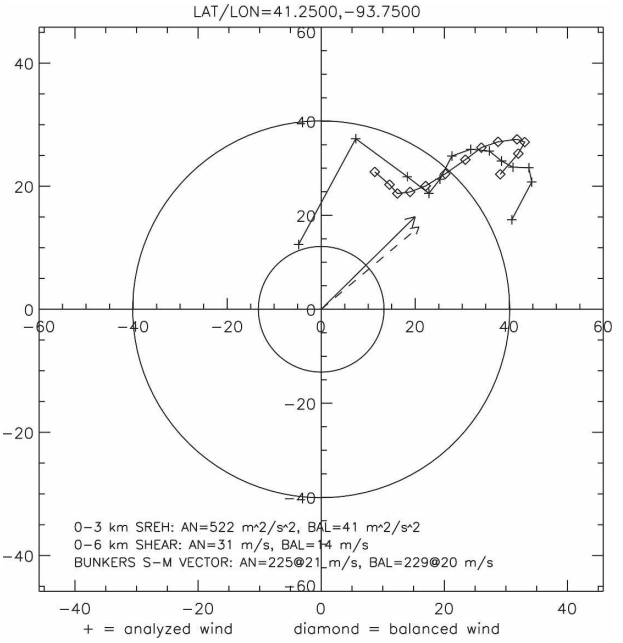

FIG. 3. Analyzed and balanced hodographs at 41.25°N, 93.75°W at 0000 UTC 8 Jun 1984. The heads of the analyzed (balanced) wind vectors are plotted as a plus sign (diamond) every 1 km from 0 km AGL (the surface) to 12 km AGL. Storm-motion vectors (SMVs) for analyzed and balanced wind profiles are also plotted (balanced SMV dashed). The values for 0–3-km SREH, 0–6-km shear, and Bunkers SMV are given below the hodographs.

b. The unbalanced PBL

The balanced diagnosis can be expected to suffer in the boundary layer, where viscous forces contribute to strong departures from geostrophy. Indeed, friction is absent from the NLB system so to the extent that the PBL wind is influenced by or (in the parlance of PV diagnosis) attributable to a PV anomaly, errors in the diagnosis will arise. Figure 3 shows a comparison of analyzed and balanced hodographs at a single grid point in the warm sector of a surface cyclone at a sample time in a major tornado outbreak, 0000 UTC 8 June 1984.

The hodographs differ greatly within the lower troposphere but are similar at altitudes greater than 1 km AGL. The differences between the near-surface analyzed and balanced winds produce equally dramatic discrepancies between analyzed and balanced SHR and SREH. The magnitude of the unbalanced lower-tropospheric flow and associated shear parameters at the grid point shown in Fig. 3 is representative of con-

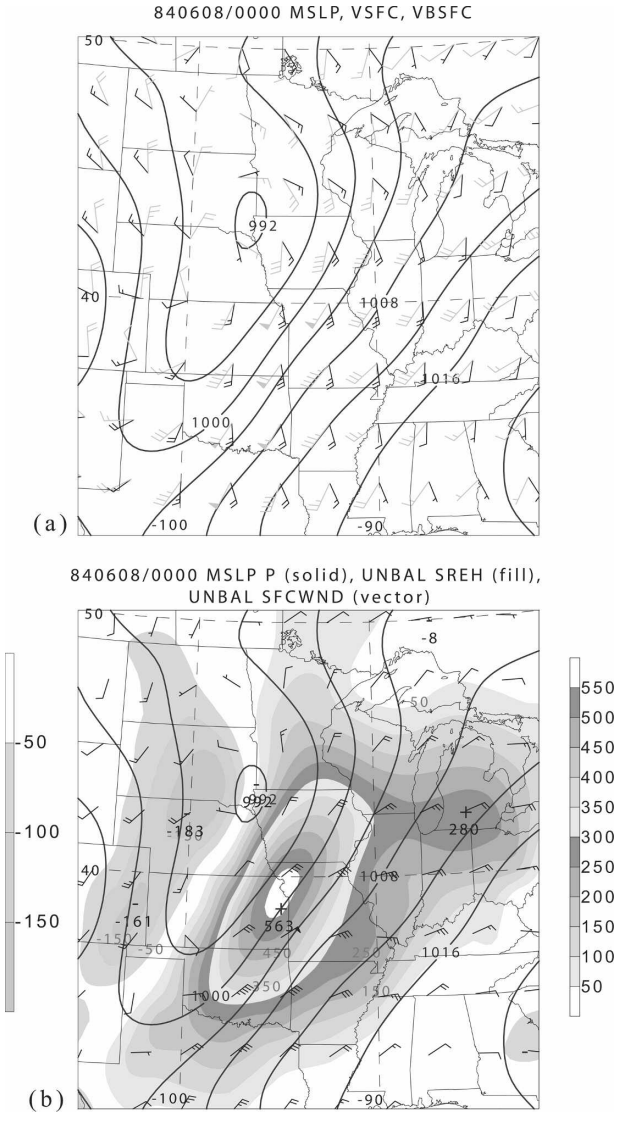

FIG. 4. (a) Analyzed vs balanced surface winds and mean sea level pressure (MSLP). Analyzed winds (kts) are plotted as black barbs. Balanced winds are plotted as larger gray barbs. MSLP (hPa) is contoured. (b) Unbalanced surface winds (analyzed minus balanced; barbs), MSLP (contours), and unbalanced 0–3-km SREH ($m^2\ s^{-2}$; shading). Left (right) vertical grayscale bar adjacent to (b) gives the shading interval levels for (negative) positive unbalanced SREH.

ditions over the entire warm sector. A comparison of analyzed ($\mathbf{V}_{\text{sfc}}$) and balanced ($\mathbf{V}_{B_{\text{sfc}}}$) surface winds at the sample time (0000 UTC 8 June 1984), presented in Fig. 4a, reveals that the latter are significantly veered (i.e., rotated clockwise) relative to the former over the warm sector, with the two wind fields differing in direction by roughly 30°–40°. The difference between analyzed and balanced SREH values (SREH − SREH_B) is correspondingly large over the same region (Fig. 4b).

PBL friction is the dominant contributor to the dramatic difference between $\mathbf{V}_{\text{sfc}}$ and $\mathbf{V}_{B_{\text{sfc}}}$ noted in Fig. 4a, and the resulting discrepancy between SREH_B and SREH displayed in Fig. 4b. The "antitriptic" wind is characterized by a balance between friction, horizontal pressure gradient, and Coriolis forces (Schaefer and Doswell 1980). Although rarely truly antitriptic, the wind field near the earth's surface is almost always affected by friction. Such a flow possesses a component oriented along the pressure gradient vector toward low pressure, as well as substantially subgeostrophic speeds. The vertically averaged analyzed PBL winds (averaged from the ground to 1 km AGL) at the sample time (Fig. 5a) across the region of interest possess a component directed toward low pressure centered over southeastern South Dakota and are uniformly weaker than the mean balanced wind, consistent with the effects of friction.

The supposition that friction is responsible for the significant imbalance in the surface winds is further supported by the close agreement between analyzed and balanced wind vectors at 1.5 km AGL, an altitude near the top of the PBL, over the central and eastern plains (Fig. 5b). The marked increase and veering of analyzed winds through the depth of the PBL implied by this close correspondence is characteristic of Ekman layers.

The lack of friction and associated PBL structure in the balanced winds do not render irrelevant a balanced diagnosis of UPV changes on the shear parameters; it is still possible to examine the effect of UPV modifications on the wind profile by computing the associated changes in the balanced flow ($\Delta\mathbf{V}_B \equiv \mathbf{V}_n - \mathbf{V}_0$) and adding them to the analyzed wind profiles to assess the impact of those changes on the balanced SHR and SREH. This technique allows one to diagnose the approximate effect of the UPV changes on the wind profile and shear parameters without limiting the analysis only to the balanced wind profiles themselves. One shortcoming of this approach is that without foreknowledge of how the PBL balanced winds are affected by friction when modified by an amount ($\Delta\mathbf{V}_B$), the true modified balanced state within the PBL cannot be known. We expect that this approach will slightly overestimate changes in shear magnitude (by roughly the same fraction that $\mathbf{V}_{B_{\text{sfc}}}$ overestimates $\mathbf{V}_{\text{PBL}}$) but that directional differences will be approximately correct.

c. *Computing the thermodynamic quantities from the balanced heights*

The objective of the current study requires using the *thermodynamic* information, in addition to the kine-

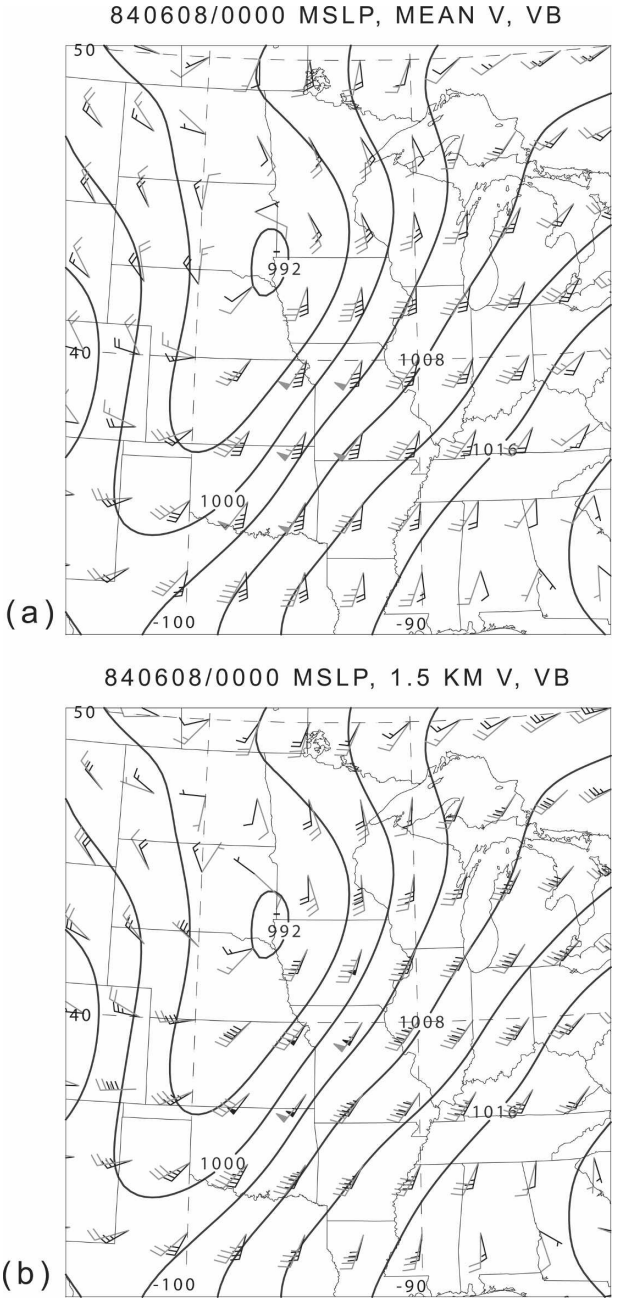

FIG. 5. (a) Mean 0–1-km analyzed and balanced winds (kt) and MSLP, and (b) 1.5-km analyzed and balanced winds and MSLP. MSLP is contoured every 4 hPa, analyzed winds are black barbs, and balanced winds are larger gray barbs.

matic fields, obtainable through PV inversion. Inverting a given PV distribution under the NLB constraint yields balanced fields Φ_B and Ψ_B over the entire inversion domain. While it is relatively straightforward to quantify the contribution of a specific PV anomaly q_i to the instantaneous vertical shear of the balanced horizontal wind through the associated partitioned streamfunction field Ψ_i, assessing the contribution of q_i to a change in CAPE requires several steps, including the retrieval of balanced virtual temperatures T_{v_B} from the balanced heights Φ_B and an "adjustment" of the mixing ratio r_B profile consistent with T_{v_B}. Moreover, the CAPE itself is a nonlinear function of temperature T and mixing ratio r, potentially complicating its interpretation in PV diagnostics.

Directly examining the link between UPV anomalies and convective destabilization, Juckes and Smith (2000) use the balanced solution for a two-dimensional shear line derived by Juckes (1999) to invert the PV (which is assumed to correspond to a situation with zero relative vorticity) approximated from observed soundings. Modified soundings are subsequently obtained for a range of idealized tropopause potential temperature perturbations $\theta'_{\rm tr}$, which is equivalent to modifying the "coupling index" (Bosart and Lackmann 1995). Juckes and Smith (2000) find that CAPE [convective inhibition (CIN)] is increased (reduced) as $\theta'_{\rm tr}$ becomes more negative and larger in horizontal scale. Rather than examining the impact of highly idealized tropopause PV anomalies on soundings (and the buoyancy parameters computed from them) within the context of an idealized two-dimensional balanced model (as do Juckes and Smith 2000), the current study seeks to reconstruct these soundings from any given analyzed or modified PV distribution using the NLB equations.

The thermodynamic parameters most commonly used to characterize the SCR are the CAPE and CIN. For a moist air parcel, the CAPE is expressed [Emanuel 1994, his Eq. (6.3.5)] as

$$\begin{aligned}\text{CAPE} &= \int_{\ln p_{\rm LNB}}^{\ln p_0} R_d (T_{v_{\rm par}} - T_v)\, d\ln p \\ &= \int_{p_{\rm LNB}}^{p_0} R_d \frac{(T_{v_{\rm par}} - T_v)}{p}\, dp, \end{aligned} \tag{7}$$

where $T_{v_{\rm par}}$ is the parcel's virtual temperature, p_0 is the parcel's origin level, and $p_{\rm LNB}$ is the parcel's level of neutral buoyancy (LNB). Expressed as a discrete sum, (7) can be approximated as

$$\text{CAPE} \approx R_d \sum_{k=1}^{N-1} (\overline{T}_{v_{{\rm par}_k}} - \overline{T}_{v_k}) \left(\frac{p_{k+1} - p_k}{p_{k+1/2}} \right), \tag{8}$$

where $\overline{(\,)}_k$ indicates logarithmic averages taken over layer (p_k, p_{k+1}), $p_{k+1/2} \equiv e^{0.5\times(\ln p_k + \ln p_{k+1})}$ and the summation in (8) is performed over all layers between the parcel origin level (taken to be the earth's surface in

this study) and the LNB. To ensure that only positive buoyancy contributes to the integral (7), the summation (8) is computed only over layers for which $\overline{T}_{v_{\mathrm{par}_k}} - \overline{T}_{v_k} > 0$; negative buoyancy is summed separately to compute the CIN.

For all CAPE and CIN calculations, $T_{v_{\mathrm{par}}}$ is found for a given pressure level by first using the difference between the parcel's pseudoadiabatic entropy and the environment's saturated pseudoadiabatic entropy [Emanuel 1994, his Eqs. (4.5.9) and (4.7.6)] to estimate a parcel temperature via $T_{\mathrm{par}} \approx T + (S_{\mathrm{par}} - S^*)(\partial T/\partial S_{\mathrm{par}})$, where the unsaturated and saturated pseudoentropies are denoted by S and S^*, respectively. The parcel's saturation vapor pressure and mixing ratio are then calculated and used to recompute S^*, which results in a smaller increment $(S_{\mathrm{par}} - S^*)$. This procedure is iterated until the entropy change is negligible, at which point the correct parcel temperature is obtained. In practice, only 5–10 iterations are necessary to achieve the desired numerical convergence. Then, the lifted parcel's mixing ratio is used to compute $T_{v_{\mathrm{par}}}$.

Computing the CAPE and CIN present in the *balanced* state requires a vertical profile of balanced layer-mean virtual temperature $\overline{T}_{v_B}$, which is given by the hypsometric equation, relating the average virtual temperature of a hydrostatically balanced fluid layer (p_k, p_{k+1}) to the thickness of that layer:

$$\overline{T}_{v_B}^{\ln p} = \frac{\Delta\Phi_B}{R_d \ln\left(\dfrac{p_k}{p_{k+1}}\right)}, \tag{9}$$

where the fluid layer is bounded beneath by pressure level k and above by level $k + 1$, and the "overbar ln p" denotes an average with respect to ln p. Given a profile of Φ_B, (9) can be used to immediately yield the corresponding balanced virtual temperature profile $\overline{T}_{v_B}$.

Since CAPE and CIN require knowledge of the parcel mixing ratio, a modified r must be estimated. The approach adopted here assumes that adjustments of T_v to the modified balanced state occur through ascent and descent, and that parcels conserve r throughout this vertical adjustment process (Fig. 6).

To illustrate the approach used in adjusting r, consider a PV change δ_q that induces the cooling of $\overline{T}_{v_B}$ within a layer. In going from the warmer to the colder balanced state, isentropic surfaces are deflected upward beneath the region where PV is modified, and parcels remain within their respective isentropic layers. As unsaturated parcels conserve their values of θ_v, they also conserve moisture. Hence, in the typical free atmospheric profile where $\partial r/\partial p > 0$, cooling is associated with moistening as parcels carry higher r values upward. At a given level, the new r is determined from the new θ_v by computing $r(\theta_v)$ from the original sounding by means of linear interpolation in θ_v. The adjustment of r, combined with the retrieval of $\overline{T}_{v_B}$ through (9), compose a procedure that is hereafter referred to as *balanced sounding reconstruction.*

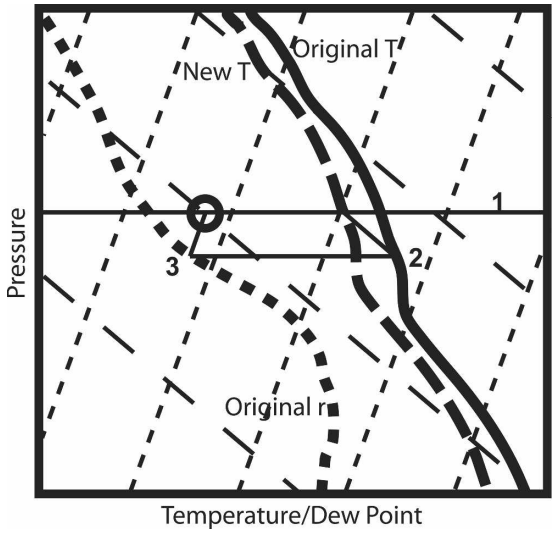

FIG. 6. Thermodynamic diagram showing original profiles of virtual temperature (thick solid) and mixing ratio (thick short dashes), and a new virtual temperature profile produced through PV inversion (thick long dashes). Background lines depict dry adiabats (thin long dashes) and lines of constant saturation mixing ratio (thin short dashes). Sounding modification is assumed to take place through vertical displacements that conserve both virtual potential temperature and mixing ratio. To obtain the new mixing ratio at a given level (1), identify the origin of the air parcel in the original sounding (2), find the mixing ratio at that level (3), and assign it to the given level in the new sounding (4).

Although the issue does not arise in the preconvective environments examined in Parts III and IV, the mixing ratio computed in this fashion may occasionally lead to supersaturation. Were this to happen, one might simply reduce r to its saturated value, but a consistent treatment of this issue (not limited to the present sounding diagram analysis) would require allowing the generation of PV through inferred diabatic heating during the static inversion of q_i.

The primary thermodynamic convective parameter considered in the remainder of this work is CAPE. The effect of PV modifications on the CIN is given little attention because CIN is more closely related to convective initiation than convective morphology and the objective of this study is to focus on how UPV changes influence the mode of convection. An explicit diagnosis of UPV changes on the CIN is postponed until Part III.

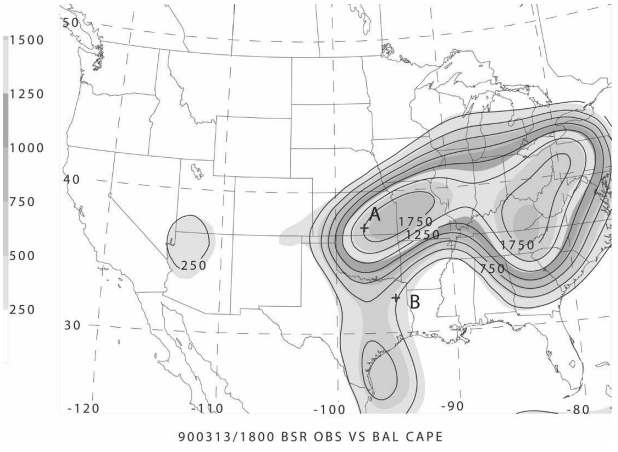

FIG. 7. CAPE (J kg^{-1}) computed from reconstructed analyzed and balanced soundings at 1800 UTC 13 Mar 1990. The analyzed CAPE distribution is shaded (fill levels given in the grayscale bar). The balanced CAPE is contoured using the same contour interval as for the analyzed distribution. Locations marked with a plus sign and labeled "A" and "B" correspond to the gridpoint soundings discussed in the text.

d. Unbalanced temperature and CAPE

Use of the balanced framework to diagnose the thermodynamic characteristics of the SCR requires that the magnitude and spatial distribution of the balanced CAPE (i.e., the CAPE computed from balanced soundings) be closely related to the actual CAPE. A comparison of CAPE computed from reconstructed analyzed soundings and balanced soundings at a sample time (1800 UTC 13 March 1990; Fig. 7) demonstrates that the two do indeed closely agree at the chosen time. The unbalanced CAPE field is the departure of the balanced CAPE distribution CAPE_B from the analyzed distribution. The maximum unbalanced CAPE magnitudes, about 10% of peak CAPE values analyzed at the sample time, can compose a significant fraction of the total CAPE near the periphery of the region possessing CAPE or at other locations where the total CAPE is small.

The agreement between full and balanced CAPE justifies proceeding with the balanced diagnosis in Parts III and IV. It is, however, of passing interest to understand the nature of the unbalanced portions of the sounding profiles and the resulting CAPE. The differences between analyzed (T) and balanced (T_B) temperature profiles and their associated CAPE values are therefore examined here at the sample time.

Figure 8 displays two superimposed soundings representing conditions at location *A* in Fig. 7. One sounding is reconstructed from the analyzed height field Φ (solid lines) and another from the balanced heights Φ_B (dashed lines). The balanced lower troposphere is generally warmer than the observations at the sample location, except for cooler temperatures in the lowest levels. Integrated below the analyzed LNB (200 hPa), however, the balanced sounding is colder, which is almost entirely attributable to colder balanced temperatures in the 400–250-hPa layer (i.e., in the upper portion of the profile possessing positive buoyancy). Thus, the balanced sounding possesses larger CAPE than is observed. Of potential importance to the assessment of convective initiation probabilities is the fact that the CIN is also larger in the balanced state because $\overline{T}_B > \overline{T}$ in the 800–575-hPa layer (Fig. 8).

At location B (Fig. 9), the balanced temperature profile is clearly *warmer* than the observations throughout most of the troposphere, leading to lower balanced CAPE. At this location, the CIN is also larger in the balanced state, so the balanced sounding might cause one to underestimate the likelihood of convection.

e. Diagnosis of imbalance

When the balanced and analyzed soundings differ at a given point, the atmospheric mass and momentum fields can be characterized as unbalanced. Specifically, the temperature differences are related to the unbalanced geopotential height field Φ' through (9). Where imbalance is present, the diagnosis of convective parameters using nonlinear balance PV inversion loses some accuracy. However, using techniques for diagnosing imbalance, locations where inaccuracies arise can be identified and accounted for.

Zhang et al. (2000) demonstrate that Φ' is approximately proportional to the total large-scale flow imbalance, as expressed by the nonlinear balance equation (Charney 1955):

$$2J(u, v) - \beta u + f\zeta - \nabla^2\Phi = \Delta\text{NBE}, \qquad (10a)$$

$$2J(u, v) - \beta u + f\zeta_{\text{ag}} = \Delta\text{NBE}. \qquad (10b)$$

If the nonlinear balance residual ΔNBE on the right-hand side (rhs) of (10a) is zero, then there exists exact balance between mass and momentum fields. If, on the other hand, the rhs of (10a) is nonzero the atmosphere is unbalanced and the degree of imbalance is quantified by the size of ΔNBE. If the wind field $\mathbf{V}$ is approximated by its nondivergent component, (10) can be rewritten in terms of the streamfunction:

$$\nabla^2\Phi = \boldsymbol{\nabla}\cdot(f\boldsymbol{\nabla}\Psi) + 2J\left(\frac{\partial\Psi}{\partial x}, \frac{\partial\Psi}{\partial y}\right) + \Delta\text{NBE}. \qquad (11)$$

After PV inversion is performed, Φ_B and Ψ_B are obtained. In practice, the actual streamfunction is nearly

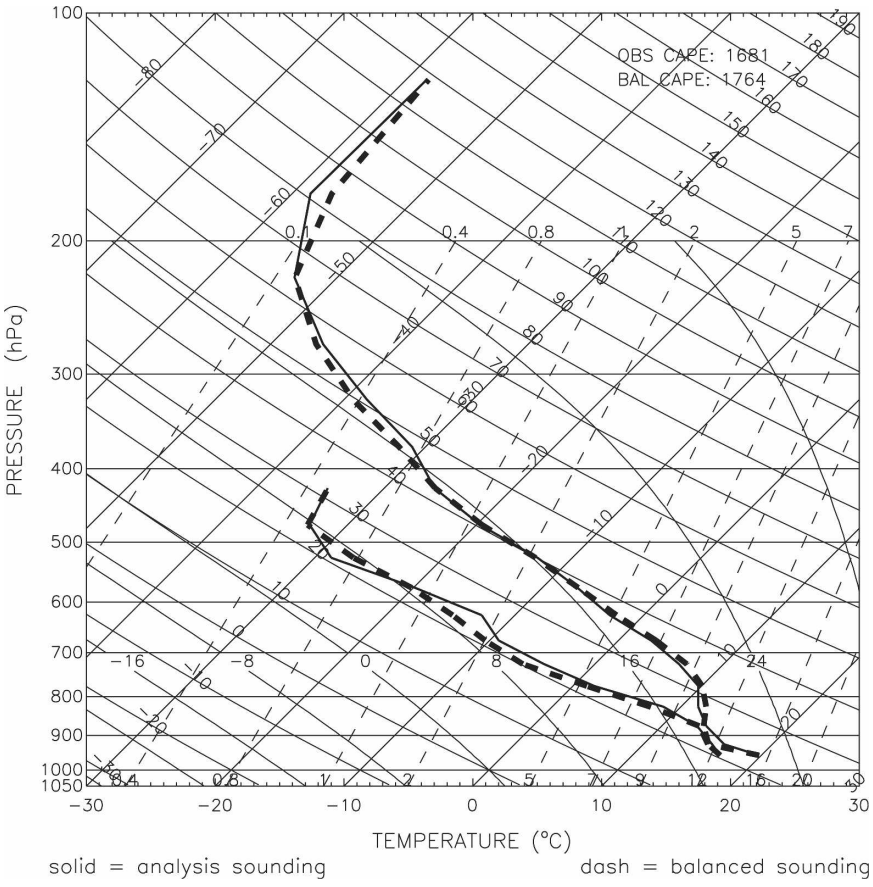

FIG. 8. Analyzed (solid) and balanced (dashed) soundings at grid point 37.5°N, 97.5°W at 1800 UTC 13 Mar 1990.

balanced but the same is *not* true for the geopotential field (Zhang et al. 2000):

$$\Psi \approx \Psi_B; \quad \Phi = \Phi_B + \Phi'. \tag{12}$$

Substituting (12) into (11), the nonlinear balance residual can be approximated by

$$\Delta\text{NBE} \approx \boldsymbol{\nabla} \cdot (f\boldsymbol{\nabla}\Psi_B) + 2J\left(\frac{\partial\psi_B}{\partial x}, \frac{\partial\psi_B}{\partial y}\right) - \nabla^2(\Phi_B) - \nabla^2(\Phi'). \tag{13}$$

By the definition of balance, the first three terms on the RHS of (13) vanish and the residual turns out to be roughly equal to the Laplacian of the unbalanced geopotential heights themselves:

$$\Delta\text{NBE} \approx \nabla^2(\Phi') \propto \Phi'. \tag{14}$$

The latter proportionality in (14) represents the common diagnostic technique of relating Laplacians of quantities to those quantities themselves. Thus, merely by inspecting distributions of Φ' it is possible to infer the spatial structure, and to a lesser degree the magnitude, of the larger-scale unbalanced flow at any atmospheric level. Moreover, an analysis of the relative sizes of the terms in (10b) makes it possible to link the breakdown of balance to particular features of the atmospheric flow in a given region.

At the sample time (1800 UTC 13 March 1990) a significant upper-level jet streak is centered over El Paso, Texas, and the exit region of this jet is located over the Texas Panhandle and western Oklahoma (Fig. 10a). The ageostrophic winds $\mathbf{V}_{ag}$ in the vicinity of the jet streak possess a strong along-stream component owing to flow curvature. Farther east over central Oklahoma and eastern Kansas, $\mathbf{V}_{ag}$ weakens considerably in proportion to the weaker geostrophic curvature there. Thus, the ageostrophic vorticity ζ_{ag} field features a maximum centered over the Oklahoma–Kansas border (Fig. 10b). A weaker minimum is evident farther east, extending southward from western Missouri into Louisiana. Inspection of the Φ' field (Fig. 10c) and comparison to the ζ_{ag} field (Fig. 10b) suggests that the flow imbalance over northwestern Oklahoma and southwestern Kansas and the weaker imbalance over Arkan-

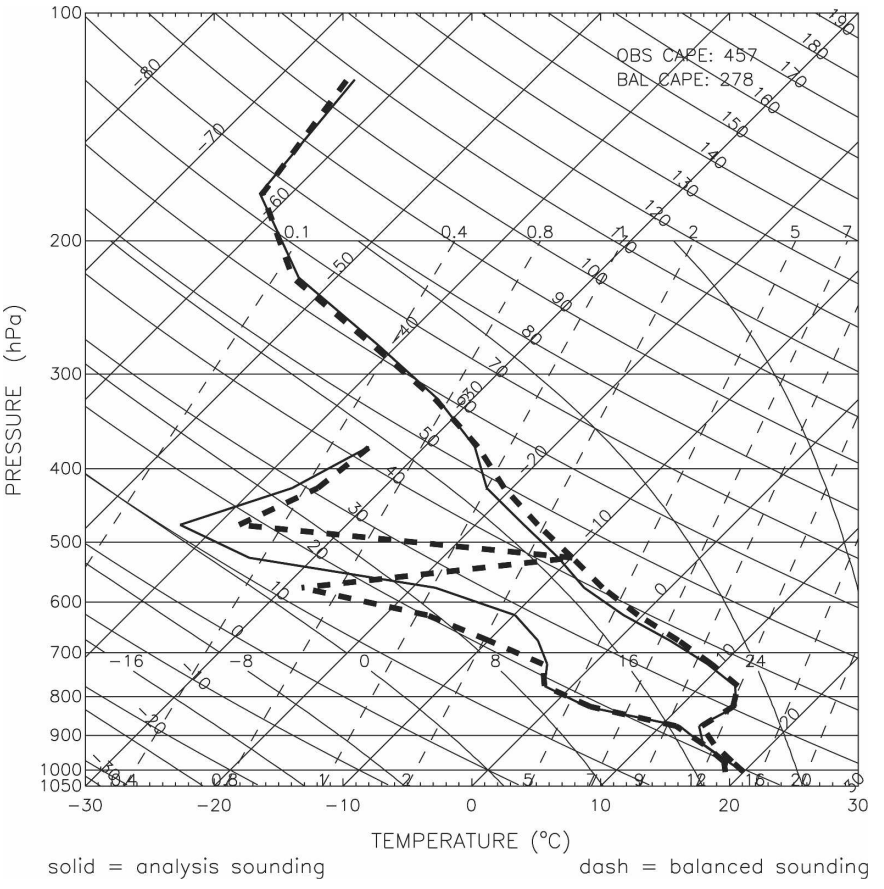

FIG. 9. Same as in Fig. 8, but at grid point 32.5°N, 95°W.

sas and Louisiana are largely attributable to the pattern of ζ_{ag}. At lower-tropospheric levels, Φ' is largely attributable to strong flow curvature within the lee trough, as evinced by the existence of a positive region of $J(u, v)$ centered over southwestern Kansas (Fig. 11a) and the corresponding positive Φ' region within the lower-tropospheric trough axis (Fig. 11b). The remaining portion of the Φ' distribution at 850 hPa southwestward over west Texas and northern Mexico is not obviously attributable to flow curvature or ζ_{ag} (not shown) and its source is not further examined here.

The unbalanced flow anomalies just examined contribute to the unbalanced CAPE anomalies shown in Fig. 10d. Thus, the vertical profiles of Φ' at the two grid points corresponding to the soundings in Fig. 8 (sounding A) and Fig. 9 (sounding B), presented in Fig. 12, explain the distribution of CAPE′ shown in Fig. 10d.

At and near the sounding A location, $\Phi' > 0$ both aloft and in the lower troposphere, but with greater magnitudes aloft, resulting in $T' \propto -\partial\Phi'/\partial p > 0$ Thus, the environmental temperature profile is generally *colder* in the balanced state, leading to larger balanced CAPE for a lifted parcel with fixed surface T and r. At location B, Φ' is slightly negative between 420 and 250 hPa (Fig. 12b) but comparatively large in the lower troposphere, resulting in a greater vertical change in Φ' than is diagnosed at location A. At location B where $-\partial\Phi'/\partial p < 0$, $T' < 0$ as well. Hence, the instantaneous flow imbalances associated with the jet streak exit region impinging on the southern plains are associated with CAPE′ < 0 in the vicinity of sounding A, representative of conditions over northern Oklahoma and central and eastern Kansas. Farther south over eastern Texas, the unbalanced CAPE anomaly is positive (i.e., CAPE′ > 0) near sounding B. Put another way, if the flow precisely obeyed nonlinear balance everywhere, the observed CAPE would likely be almost 100 J kg^{-1} higher at sounding location A and nearly 200 J kg^{-1} lower at sounding location B. The larger unbalanced CAPE over region B is attributable to the stronger vertical gradient of Φ' there. Similar investigations of the unbalanced flow at various times in various cases using (10), none of which are detailed here, revealed that it is not always possible to find meaningful correspondence between ζ_{ag} and Φ', or between $J(u, v)$ and Φ'. Even when there exists no obvious link between unbalanced

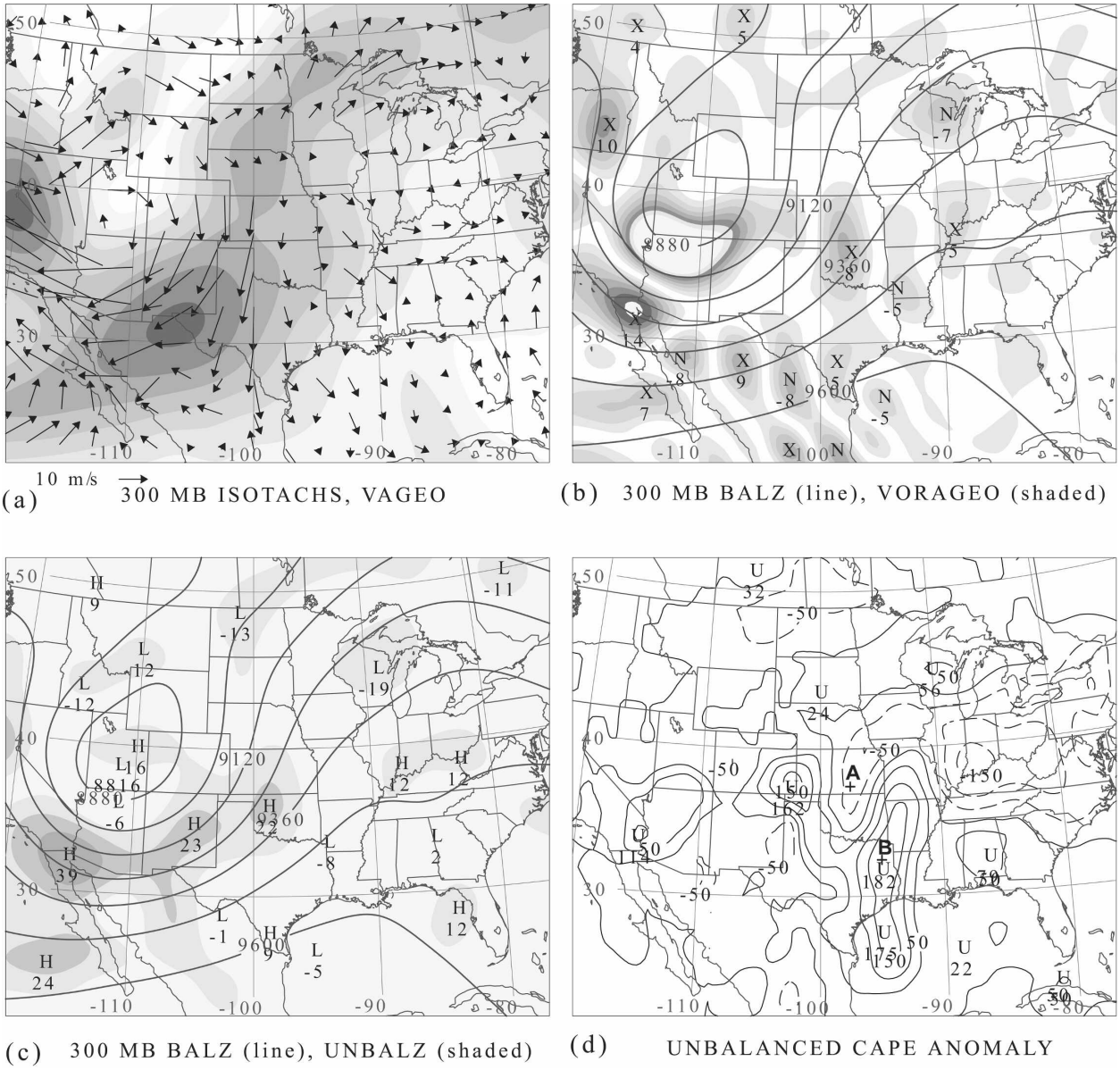

FIG. 10. Unbalanced and ageostrophic quantities at 300 hPa at 1800 UTC 13 Mar 1990. (a) Isotachs (m s^{-1}, shading) and ageostrophic wind vectors (m s^{-1}, arrows); (b) ageostrophic vorticity (s^{-1}, shading) and Φ_B (m, contours) at 300 hPa; (c) Φ' (m; shading) and Φ_B (m; contours); (d) unbalanced CAPE (J kg^{-1}; total CAPE minus balanced CAPE). Points marked "A" and "B" in (d) denote locations of gridpoint soundings shown in Figs. 8a and 9a, respectively.

CAPE and identifiable atmospheric structures, balanced diagnosis can proceed provided that the unbalanced CAPE field is not comparable in magnitude to the observed CAPE over the region of interest.

4. Summary

The basis for the current study is the notion that one can use PV inversion to diagnose the effect on thermodynamic and wind profiles of changes in the structure and/or amplitude of upper-tropospheric troughs. This paper presents a framework by which the upper-tropospheric PV distribution can be linked directly to the severe convective parameter space. The procedure for doing so involves specifying the particular PV perturbation to be investigated and quantifying its contribution to the balanced flow fields and its corresponding impact on the various convective parameters.

Because the method deals with PV perturbations, the background state for the inversion is just the model

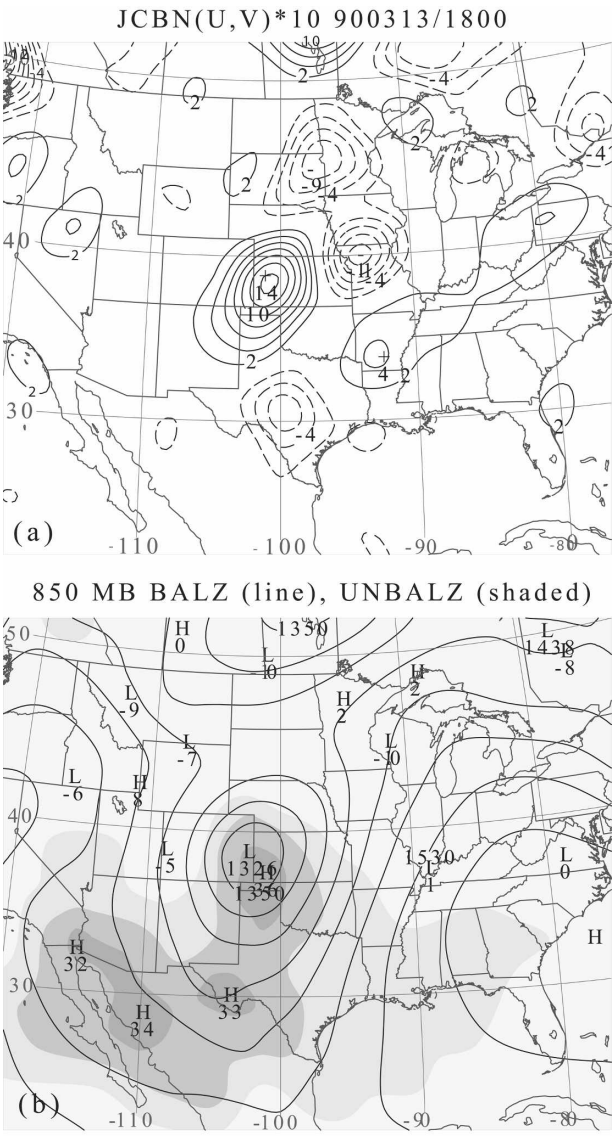

FIG. 11. Nonlinear forcing term in the balance equation and unbalanced heights at 850 hPa at 1800 UTC 13 Mar 1990. (a) Jacobian of the analyzed winds at 850 hPa (10^{-10} s^{-2}). (b) Balanced (contour) and unbalanced (shading) heights (m).

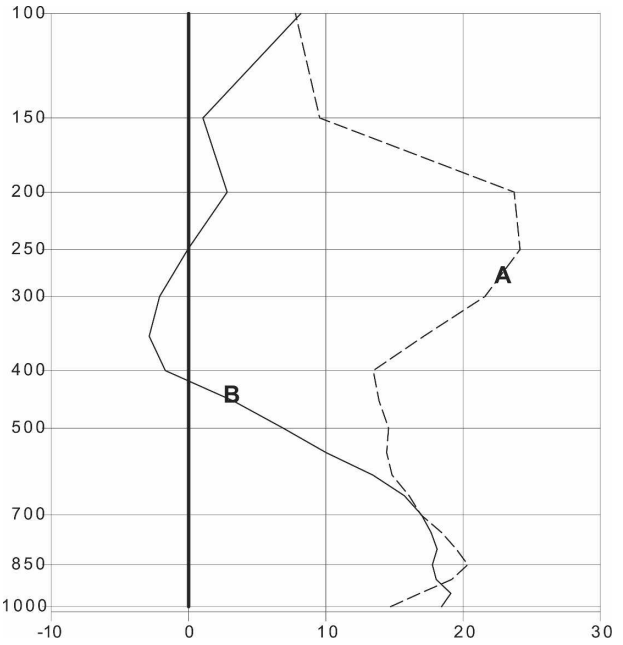

FIG. 12. Vertical profiles of Φ'. Profiles shown are located at 32.5°N, 95°W (solid line, corresponding to sounding B in Fig. 8a) and 37.5°N, 97.5°W (dashed line, sounding A in Fig. 9a). A solid vertical line highlights the $x = 0$ m unbalanced height value.

forecast or analysis itself. Full inversions are carried out with the original and modified PV. PV modifications are made that mimic the effect of localized lateral displacements of the dynamic tropopause. Moisture is necessary for convective diagnosis but is not directly recoverable from PV inversion. Moisture modifications are made by assuming that the vertical displacement of isentropic surfaces between the original and modified balanced states corresponds to the vertical displacement of mixing ratio–conserving air parcels. Other aspects of the atmospheric state are unbalanced, and since such aspects may contribute significantly to variations in convective parameters, those issues were considered here.

Departures from balance can cause differences between the balanced CAPE and full CAPE. Unbalanced CAPE anomalies are associated with small unbalanced environmental temperature differences distributed throughout a deep tropospheric layer. The differences between analyzed and balanced soundings are, in certain regions, attributable to recognizable upper-tropospheric flow features (e.g., an unbalanced jet exit region). The largest diagnosed unbalanced CAPE magnitudes rarely exceed 10% of the peak warm sector CAPE values, so in practice the existence of unbalanced CAPE will not jeopardize the overall interpretation of the balanced CAPE diagnosis, except possibly near the boundaries of the CAPE distribution.

The methodology described here is a general one for diagnosing the instantaneous relationship between PV anomalies and sounding characteristics. The immediate motivation for developing these techniques was to diagnose the sensitivity to details of the upper-tropospheric flow of some key sounding parameters used to diagnose severe convection. The next step in this study (Part II) is to use PV inversion of idealized anomalies to understand the nature of the changes to the shear and temperature profiles. With both technical and conceptual tools in place, we proceed to diagnose the sensitivity of sounding parameters in two major tornado

outbreaks involving possibly important upper-tropospheric shortwaves (Parts III and IV).

Boundary layer winds are shown here to be largely unbalanced owing to the neglect of friction in the balanced framework. In the context of environments supporting severe convection, the hallmark of this imbalance is the absence from balanced hodographs of the strongly veering PBL wind profile commonly observed in the warm sector of Great Plains cyclones. Accordingly, balanced SREH and SHR values are negligibly small in the warm sector, whereas the observed warm sector values are comparatively large. In light of this limitation of the balanced diagnosis, the case study analyses will avoid dealing directly with the balanced shear parameters. Rather than comparing the balanced and analyzed shear parameters (as is done for the CAPE), changes in the shear parameters will be quantified from *modified* analyzed hodographs. These hodographs, in turn, are obtained by adding to the analyzed vertical wind profile the profile of balanced wind changes attributable to a given PV modification.

Acknowledgments. The authors thank Christopher Davis for providing the software used in inverting the PV, as well as for providing invaluable assistance with the use of the prognostic balance equation solver. This research was supported by the National Science Foundation through Grant ATM-0089906.

REFERENCES

Bosart, L. F., and G. M. Lackmann, 1995: Postlandfall tropical cyclone reintensification in a weakly baroclinic environment: A case study of Hurricane David (September 1979). *Mon. Wea. Rev.,* **123,** 3268–3291.

Bunkers, M. J., B. A. Klimowski, J. W. Zeitler, R. L. Thompson, and M. L. Weisman, 2000: Predicting supercell motion using a new hodograph technique. *Wea. Forecasting,* **15,** 61–79.

Charney, J. G., 1955: The use of primitive equations of motion in numerical prediction. *Tellus,* **7,** 22–26.

Craven, J. P., H. E. Brooks, and J. A. Hart, 2002: Baseline climatology of sounding derived parameters associated with deep, moist convection. Preprints, *21st Conf. on Severe Local Storms,* San Antonio, TX, Amer. Meteor. Soc., 643–646.

Daubechies, I., 1992: *Ten Lectures on Wavelets.* Society for Industrial and Applied Mathematics, 357 pp.

Davies, J. M., and R. H. Johns, 1993: Some wind and instability parameters associated with strong and violent tornadoes. 1. Wind shear and helicity. *The Tornado: Its Structure, Dynamics, Prediction, and Hazards, Geophys. Monogr.,* Vol. 79, Amer. Geophys. Union, 573–582.

Davis, C. A., and K. A. Emanuel, 1991: Potential vorticity diagnostics of cyclogenesis. *Mon. Wea. Rev.,* **119,** 1929–1953.

——, and L. F. Bosart, 2002: Numerical simulations of the genesis of Hurricane Diana (1984). Part II: Sensitivity of track and intensity prediction. *Mon. Wea. Rev.,* **130,** 1100–1124.

——, E. D. Grell, and M. A. Shapiro, 1996: The balanced dynamical nature of a rapidly intensifying oceanic cyclone. *Mon. Wea. Rev.,* **124,** 3–26.

Dickinson, M. J., L. F. Bosart, W. E. Bracken, G. J. Hakim, D. M. Schultz, M. A. Bedrick, and K. R. Tyle, 1997: The March 1993 Superstorm cyclogenesis: Incipient phase synoptic- and convective-scale flow interaction and model performance. *Mon. Wea. Rev.,* **125,** 3041–3072.

Done, J., C. A. Davis, and M. Weisman, 2004: The next generation of NWP: Explicit forecasts of convection using the weather research and forecasting (WRF) model. *Atmos. Sci. Lett.,* **5,** 110–117.

Doswell, C. A., III, 1982: The operational meteorology of convective weather, Vol. I: Operational mesoanalysis. NOAA Tech. Memo. NWS NSSFC-5, Kansas City, MO, 164 pp.

——, 1987: The distinction between large-scale and mesoscale contribution to severe convection: A case study example. *Wea. Forecasting,* **2,** 3–16.

Emanuel, K. A., 1994: *Atmospheric Convection.* Oxford University Press, 592 pp.

Fowle, M. A., and P. J. Roebber, 2003: Short-range (0–48 h) numerical prediction of convective occurrence, mode, and location. *Wea. Forecasting,* **18,** 782–794.

Gold, D. A., 2004: A potential vorticity diagnosis of the relationship between upper-level troughs and the severe convective regime. Ph.D. thesis, Texas A&M University, 194 pp.

——, and J. W. Nielsen-Gammon, 2008a: Potential vorticity diagnosis of the severe convective regime. Part III: The Hesston tornado outbreak. *Mon. Wea. Rev.,* **136,** 1593–1611.

——, and ——, 2008b: Potential vorticity diagnosis of the severe convective regime. Part IV: Comparison with modeling simulations of the Moore tornado outbreak. *Mon. Wea. Rev.,* **136,** 1612–1629.

Hoskins, B. J., M. E. McIntyre, and A. W. Robertson, 1985: On the use and significance of isentropic potential vorticity maps. *Quart. J. Roy. Meteor. Soc.,* **111,** 877–946.

Huo, Z., D.-L. Zhang, and J. R. Gyakum, 1999: Interaction of potential vorticity anomalies in extratropical cyclogenesis. Part II: Sensitivity to initial perturbations. *Mon. Wea. Rev.,* **127,** 2563–2575.

Johns, R., and J. A. Hart, 1993: Differentiating between types of severe thunderstorm outbreaks: A preliminary investigation. Preprints, *17th Conf. on Severe Local Storms,* St. Louis, MO, Amer. Meteor. Soc., 46–50.

Juckes, M., 1999: The structure of idealized upper-tropospheric shear lines. *J. Atmos. Sci.,* **56,** 2830–2845.

——, and R. K. Smith, 2000: Convective destabilization by upper-level troughs. *Quart. J. Roy. Meteor. Soc.,* **126,** 111–123.

Kalnay, E., and Coauthors, 1996: The NCEP/NCAR 40-Year Reanalysis Project. *Bull. Amer. Meteor. Soc.,* **77,** 437–471.

Mesinger, F., and R. E. Treadon, 1995: "Horizontal" reduction of pressure to sea level: Comparison against the NMC's Shuell method. *Mon. Wea. Rev.,* **123,** 59–68.

Nielsen-Gammon, J. W., and R. Lefevre, 1996: Piecewise tendency diagnosis of dynamical processes governing the development of an upper-tropospheric mobile trough. *J. Atmos. Sci.,* **53,** 3120–3142.

——, and D. A. Gold, 2008: Potential vorticity diagnosis of the severe convective regime. Part II: The impact of idealized PV anomalies. *Mon. Wea. Rev.,* **136,** 1582–1592.

Rasmussen, E. N., and D. O. Blanchard, 1998: A baseline climatology of sounding-derived supercell and tornado forecast parameters. *Wea. Forecasting,* **13,** 1148–1164.

Roebber, P. J., D. M. Schultz, and R. Romero, 2002: Synoptic regulation of the 3 May 1999 tornado outbreak. *Wea. Forecasting,* **17,** 399–429.

Schaefer, J. T., 1986: Severe thunderstorm forecasting: A historical perspective. *Wea. Forecasting,* **1,** 164–189.

——, and C. A. Doswell, 1980: The theory and practical application of antitriptic balance. *Mon. Wea. Rev.,* **108,** 746–756.

Thompson, R. L., and R. Edwards, 2000: An overview of environmental conditions and forecast implications of the 3 May 1999 tornado outbreak. *Wea. Forecasting,* **15,** 682–699.

Weisman, M. L., and J. B. Klemp, 1982: The dependence of numerically simulated convective storms on vertical wind shear and buoyancy. *Mon. Wea. Rev.,* **110,** 504–520.

Zhang, F., S. E. Koch, C. A. Davis, and M. L. Kaplan, 2000: A survey of unbalanced flow diagnostics and their application. *Adv. Atmos. Sci.,* **17,** 165–183.